An observational radiative constraint on hydrologic cycle intensification

A. M. DeAngelis, X. Qu, M. D. Zelinka, A. Hall

July 28, 2017

Disclaimer

This document was prepared as an account of work sponsored by an agency of the United States government. Neither the United States government nor Lawrence Livermore National Security, LLC, nor any of their employees makes any warranty, expressed or implied, or assumes any legal liability or responsibility for the accuracy, completeness, or usefulness of any information, apparatus, product, or process disclosed, or represents that its use would not infringe privately owned rights. Reference herein to any specific commercial product, process, or service by trade name, trademark, manufacturer, or otherwise does not necessarily constitute or imply its endorsement, recommendation, or favoring by the United States government or Lawrence Livermore National Security, LLC. The views and opinions of authors expressed herein do not necessarily state or reflect those of the United States government or Lawrence Livermore National Security, LLC, and shall not be used for advertising or product endorsement purposes.

An observational radiative constraint on hydrologic cycle intensification

Anthony M. DeAngelis[1*], Xin Qu[1], Mark D. Zelinka[2], Alex Hall[1]

[1]Department of Atmospheric and Oceanic Sciences, University of California Los Angeles, Los Angeles, CA 90095

[2]Program for Climate Model Diagnosis and Intercomparison, Lawrence Livermore National Laboratory, Livermore, CA 94550

*Corresponding author:

Anthony M. DeAngelis
Department of Atmospheric and Oceanic Sciences
University of California, Los Angeles
PO Box 951565
Los Angeles, CA 90095-1565, USA
Phone: 310-206-5257
Fax: 310-206-5219

E-mail: adeangelis@ucla.edu

32   **Main Text**

33

34   **Hydrologic cycle intensification is a key dimension of climate change, with**

35   **significant impacts on human and natural systems[1,2]. A basic measure of hydrologic cycle**

36   **intensification, the increase in global-mean precipitation per unit surface warming, varies**

37   **by a factor of three in current-generation climate models (~1-3 % K^{-1})[3-5]. We show that a**

38   **substantial portion of this spread can be traced to intermodel variations in the atmospheric**

39   **shortwave absorption response to warming. As climate warms, increases in shortwave**

40   **absorption suppress the precipitation increase by reducing the latent heating increase**

41   **required to keep the atmospheric energy budget balanced[6,7]. Spread in the shortwave**

42   **absorption response can be explained by differences in the sensitivity of solar absorption to**

43   **variations in column precipitable water. An observational estimate suggests that in many**

44   **models, this sensitivity is too small, and that the shortwave absorption response to warming**

45   **is too weak. Spread in the simulated sensitivity of solar absorption to varying water vapor**

46   **concentration is linked to differences in radiative transfer parameterizations. Attaining**

47   **accurate shortwave absorption responses through radiative transfer scheme improvement**

48   **could reduce spread in global precipitation increase per unit warming at the end of the 21st**

49   **century by ~35%, and produce an ensemble-mean increase that is almost 40% smaller.**

50   Although local precipitation changes are relevant for direct societal impacts, the change

51   in globally-averaged precipitation is a first-order indicator of climate change that must be well

52   understood and accurately simulated. Evaluation of model-simulated global precipitation change

53   with actual precipitation observations is difficult due to uncertainties and insufficient spatial and

54 temporal data coverage[8]. An alternative approach is to understand and evaluate it through

55 consideration of the physical processes that govern it.

56 Projected global-mean precipitation changes are dictated by the atmospheric energy

57 budget's response to imposed radiative forcing and subsequent surface and atmospheric

58 changes[5-7,9,10]. On annual and longer timescales, net atmospheric longwave cooling to the

59 surface and outer space (LWC) is balanced by heating from shortwave absorption (SWA),

60 sensible heating from the surface (SH), and latent heat release from precipitation (L_vP, latent heat

61 of vaporization multiplied by precipitation rate) according to the following[11] (see also Fig. 1):

$$LWC = L_vP + SWA + SH \tag{1}$$

63 When carbon dioxide (CO_2) and other greenhouse gases increase, and the planet warms, these

64 energy sources and sinks readjust due to a series of surface and atmospheric changes. Upon

65 reaching equilibrium, the new balance is characterized by enhanced longwave cooling, increased

66 solar absorption, decreased sensible heat flux from surface to atmosphere, and increased

67 precipitation[6,11-13] (Fig. 1b). Climate model differences in the relative changes in the radiative

68 and SH terms, per unit surface warming, produce different global-mean precipitation

69 responses[7,12,14]. While it is clear that SWA increases mainly due to Clausius-Clapyeron-driven

70 increases in atmospheric water vapor, previous studies have demonstrated that the SWA response

71 to warming has a notable spread across models[4,7,12]. Moreover, the physical basis for this spread

72 and extent to which it can explain spread in the precipitation response remains a topic of

73 debate[4,7,12].

74 Global-mean precipitation responds to CO_2 forcing on two timescales[9,15], as illustrated by

75 idealized experiments where CO_2 suddenly increases. Precipitation initially decreases due to a

76 rapid increase in atmospheric static stability resulting from suppressed longwave cooling (the

77   rapid adjustment)[16,17], then slowly increases with subsequent global-mean surface warming (the

78   temperature-mediated response)[18,19]. Previous studies investigating intermodel spread in the

79   global-mean precipitation response to increased CO_2 have either not considered rapid

80   adjustments and temperature-mediated responses separately (i.e., they analyzed total

81   precipitation changes)[4,12], or analyzed a relatively small number of models, undersampling the

82   ensemble[7]. These limitations have hindered understanding of the sources of spread in hydrologic

83   cycle intensification, particularly regarding the role of shortwave absorption[4,7]. Here, we analyze

84   rapid and temperature-mediated responses of global precipitation to CO_2 forcing in 25 models

85   participating in the Coupled Model Intercomparison Project Phase 5 (CMIP5) to understand the

86   spread.

87   Rapid adjustments and temperature-mediated responses are separated by regressing

88   globally-averaged annual anomalies in the atmospheric energy budget terms of Equation 1

89   against surface air temperature (T) anomalies in simulations of instantaneous CO_2 quadrupling

90   (Methods). For each term, the regression slope represents the temperature-mediated response

91   (hereafter dX/dT, where $X = [L_vP, SWA, LWC,$ or $SH]$) and the y-intercept where $\Delta T=0$ is the

92   rapid adjustment[20] (Extended Data Fig. 1). The temperature-mediated precipitation response,

93    $L_v dP/dT$, exhibits substantial intermodel spread, with values ranging from ~1.8 to 2.7

94   W m^{-2} K^{-1} [2.0-3.2 % K^{-1}] (Fig. 2a). This would contribute a 4.5 W m^{-2} spread in total L_vP

95   change, the difference between a 10% and a 16% increase, if all models were to warm by ~5 K

96   (the multi-model mean warming averaged ~140-150 years after CO_2 quadrupling). The spread in

97   total L_vP change resulting from the rapid adjustment from the same forcing is smaller (~3 W m^{-2})

98   (Extended Data Fig. 3). In this work, we focus on understanding spread in the temperature-

99   mediated component.

100   While longwave cooling is the key driver of temperature-mediated precipitation change

101   in the multi-model mean, the spread in $dLWC/dT$ and $dSWA/dT$ is large, and each accounts for

102   substantial intermodel spread in $L_v dP/dT$ (|r|>0.60) (Extended Data Fig. 2).   The anti-

103   correlation between $dSWA/dT$ and $L_v dP/dT$ is somewhat larger in magnitude and occurs in

104   both all-sky (r=-0.64) and clear-sky (r=-0.73) (Fig. 2a). This suggests clouds play a negligible

105   role in the relationship[7,10] (Extended Data Fig. 2b). An anti-correlation arises because *SWA* and

106   *$L_v P$* compete to balance enhanced longwave cooling in a warmer climate (Fig. 1). Thus models

107   with a larger *SWA* increase tend to have a smaller *$L_v P$* increase, per unit surface warming. The

108   importance of solar absorption for model spread in the global-mean precipitation response to

109   increased CO_2 was also demonstrated by ref. [7]; however, we find the importance of solar

110   absorption stems mainly from the temperature-mediated component of the change, inconsistent

111   with their findings (Methods). Based on our results, $dSWA/dT$ is a key source of model spread

112   in hydrologic cycle intensification, analogous to the importance of cloud feedbacks for model

113   uncertainty in climate sensitivity.

114   What generates the spread in $dSWA/dT$? Under greenhouse-gas induced warming, *SWA*

115   increases mainly due to enhanced solar absorption by water vapor in a warmer and moister

116   atmosphere[7,12].   Thus, model spread in $dSWA/dT$ arises from differences in water vapor

117   absorption. This is supported by the large anti-correlation between $L_v dP/dT$ and clear-sky

118     $dSWA/dT$ (Fig. 2b).   Previous studies have proposed two potential sources of model

119   disagreement in the simulated increase of solar absorption: 1) different increases in global-mean

120   column water vapor and/or different vertical/horizontal patterns of vapor change for the same

121   surface warming[7]; 2) differences in the sensitivity of solar absorption to a unit change in

122   atmospheric water vapor content, related to radiative transfer parmeterizations[12]. In this paper,

123   we seek to determine which source is more important and to better understand its physical basis.

124   We focus on clear-sky *SWA*, and hereafter, *SWA* will refer to its clear-sky component.

125   Does model spread in $dSWA/dT$ come from the first source, i.e., differences in the water

126   vapor response for the same surface warming? Cross-model correlations between globally-

127   averaged temperature-mediated water vapor responses (both column-integrated and at individual

128   levels) and $dSWA/dT$ are weak and statistically insignificant, suggesting it does not (Methods,

129   Extended Data Fig. 4). To substantiate this further and examine the role of horizontal variability

130   in vapor changes, we estimate $dSWA/dT$ using radiative kernels, i.e., linear approximations of

131   radiative flux sensitivity to perturbations in atmospheric state (Methods). As the kernels are

132   developed with a single radiative transfer code[14], model spread in kernel-derived $dSWA/dT$

133   mainly reflects intermodel differences in the water vapor response to surface warming[14]. If the

134   vapor response were causing most of the spread in $dSWA/dT$, the kernel-derived $dSWA/dT$ and

135   actual $dSWA/dT$ computed from model-produced fluxes should be highly correlated, with a

136   similar spread. However, kernel-derived $dSWA/dT$ exhibits approximately half the spread and

137   is uncorrelated with model-produced $dSWA/dT$ (Fig. 2a). Thus model variations in $dSWA/dT$

138   are unaccounted for by the total water vapor increase or subtle differences in the

139   vertical/horizontal structure of vapor increase among models. This is consistent with the

140   findings of ref. [12]. Instead, the main source of intermodel variability in $dSWA/dT$ would

141   appear to be the sensitivity of solar absorption to a unit change in atmospheric water vapor.

142   The sensitivity of solar absorption to a change in water vapor concentration is estimated

143   in each model by binning clear-sky *SWA* based on local-monthly column precipitable water (*PW*)

144   in the control climate and computing the regression slope of bin-averaged *SWA* against *PW*

145   (Methods). This quantity is hereafter denoted as $dSWA/dPW$. Fig. 3a shows *SWA* versus *PW*

6

146 curves for the two models having the largest and smallest sensitivity. $dSWA/dPW$ ranges from

147 0.03 to 0.11 %/[kg m^{-2}] across models (Fig. 3), with much of the difference arising from

148 absorption under moist conditions (Extended Data Fig. 5). $dSWA/dPW$ is almost perfectly

149 correlated with $dSWA/dT$ across models (r=0.93, Fig. 3b). This confirms that the sensitivity of

150 solar absorption to a change in atmospheric moisture is the principal source of spread in the

151 temperature-mediated *SWA* response to CO_2 forcing.

152 We estimate the real atmosphere's $dSWA/dPW$ by combining radiative fluxes from the

153 Clouds and the Earth's Radiant Energy System Energy Balance and Filled products (CERES-

154 EBAF)[21,22] with *PW* measurements from three sources (Methods). $dSWA/dPW$ obtained from

155 CERES-EBAF and each *PW* dataset (~0.11-0.13 %/[kg m^{-2}]) is on the upper end of the CMIP5

156 range (Fig. 3), implying that $dSWA/dPW$ is too weak in most models. This is consistent with

157 recent studies showing that many climate models underestimate solar absorption in moist

158 atmospheres[23-25]. Thus the temperature-mediated *SWA* response is underestimated by many

159 models. Models with $dSWA/dPW$ within statistical uncertainty of observations have $dSWA/dT$

160 ranging from 0.95-1.09 W m^{-2} K^{-1}, i.e. the upper 25% of the full spread of 0.52-1.09 W m^{-2} K^{-1}

161 (Fig. 3b). Given the strong anti-correlation between $dSWA/dT$ and $L_v dP/dT$ (Fig. 2b), this

162 further implies that many models *overestimate* the temperature-mediated increase in global-mean

163 precipitation, assuming no compensating errors in other energy budget terms. This assumption

164 may not be true, however, as models may underestimate projected increases in longwave cooling

165 because of a hypothesized missing iris effect[26]. If this is the case, it would contribute an

166 *underestimation* in global precipitation increase that is independent of temperature-mediated

167 shortwave absorption (Methods).

168 What is the physical basis for the model spread in $dSWA/dPW$? Simulated solar

169 absorption for a given atmospheric water vapor concentration is determined by radiative transfer

170 algorithms that approximate complex spectral absorption by water vapor molecules, among other

171 constituents. We examine the influence of these algorithms on simulated $dSWA/dPW$ by

172 categorizing the shortwave parameterization scheme in each model based on its treatment of

173 clear-sky solar absorption by water vapor (Fig. 4). The schemes vary considerably among

174 models and their characteristics have a strong correspondence with $dSWA/dPW$. In general,

175 models that implement more modern approaches and/or use a larger number of mathematical

176 terms (N in Fig. 4) to approximate the complex dependency of shortwave transmission on

177 wavelength, tend to have larger and more realistic $dSWA/dPW$ (see also Methods). It is

178 important to note that a commonly used observational product, the International Satellite Cloud

179 Climatology flux dataset (ISCCP-FD)[27], exhibits a large bias in $dSWA/dPW$ (Fig. 4). This

180 product generates fluxes with a radiative transfer algorithm nearly identical to that used in the

181 GISS-E2-H and GISS-E2-R models (Methods), and as a consequence yields the same

182 $dSWA/dPW$ as those models. Thus, caution should be taken when treating ISCCP-FD radiative

183 fluxes as observations.

184 Intermodel variability in the accuracy of shortwave parameterization schemes likely

185 results from model developers' ongoing challenge of balancing the need for accurate radiative

186 transfer calculations against considerations of computational efficiency and realistic simulation

187 of other climate system components[24]. As computational capabilities have grown, improvement

188 in longwave schemes and other model components (e.g., cloud processes) seem to have taken

189 precedence over parameterization of shortwave gaseous absorption, with many modeling

190 institutions continuing to implement outdated schemes for the latter in CMIP5[24,25,28] (Extended

8

191 Data Fig. 6). This is understandable considering the importance of cloud feedbacks and

192 longwave fluxes and for climate sensitivity, but here we show that atmospheric solar absorption

193 is equally important for hydrologic cycle intensification. Based on a simple calculation

194 (Methods), we estimate that if the temperature-mediated SWA response to CO_2 forcing were

195 perfectly constrained in the current generation of models, the spread in total precipitation

196 increase per unit warming predicted at the end of the 21st century under the Representative

197 Concentration Pathway scenario 8.5 (RCP8.5)[29] could be reduced by ~35%, and the ensemble-

198 mean precipitation increase per unit warming would decrease by nearly 40% (Extended Data Fig.

199 7). Even for the total precipitation change (i.e. not normalized by surface warming), a spread

200 reduction of ~25% and reduction in ensemble-mean increase of ~25% could be obtained.

201 Clearly, shortwave radiative transfer parameterizations need improvement in many climate

202 models, and fortunately, this is already underway at several modeling institutions[25].

203

204 **References**

205

206 1. Trenberth, K. E. Changes in precipitation with climate change. *Clim. Res.* **47**, 123-138

207   (2011).

208 2. Pendergrass, A. G. & Hartmann, D. L. Changes in the distribution of rain frequency and

209   intensity in response to global warming. *J. Clim.* **27**, 8372-8383 (2014).

210 3. Kharin, V. V., Zwiers, F. W., Zhang, X. & Wehner, M. Changes in temperature and

211   precipitation extremes in the CMIP5 ensemble. *Clim. Change* **119**, 345-357 (2013).

212 4. Pendergrass, A. G. & Hartmann, D. L. Global-mean precipitation and black carbon in AR4

213   simulations. *Geophys. Res. Lett.* **39**, L01703 (2012).

214 5. Andrews, T. & Forster, P. M. The transient response of global-mean precipitation to increasing carbon dioxide levels. *Environ. Res. Lett.* **5**, 025212 (2010).

216 6. O'Gorman, P. A., Allan, R. P., Byrne, M. P. & Previdi, M. Energetic constraints on precipitation under climate change. *Surv. Geophys.* **33**, 585-608 (2012).

218 7. Takahashi, K. The global hydrological cycle and atmospheric shortwave absorption in climate models under CO2 forcing. *J. Clim.* **22**, 5667-5675 (2009).

220 8. Arkin, P. A., Smith, T. M., Sapiano, M. R. P. & Janowiak, J. The observed sensitivity of the global hydrological cycle to changes in surface temperature. *Environ. Res. Lett.* **5**, 035201 (2010).

223 9. Allen, M. R. & Ingram, W. J. Constraints on future changes in climate and the hydrologic cycle. *Nature* **419**, 224-232 (2002).

225 10. Lambert, F. H. & Webb, M. J. Dependency of global mean precipitation on surface temperature. *Geophys. Res. Lett.* **35**, L16706 (2008).

227 11. Manabe, S. & Wetherald, R. T. The effects of doubling the CO_2 concentration on the climate of a general circulation model. *J. Atmos. Sci.* **32**, 3-15 (1975).

229 12. Pendergrass, A. G. & Hartmann, D. L. The atmospheric energy constraint on global-mean precipitation change. *J Clim.* **27**, 757-768 (2014).

231 13. Mitchell, F. B., Wilson, C. A. & Cunnington, W. M. On CO_2 climate sensitivity and model dependence of results. *Q. J. R. Meteorol. Soc.* **113**, 293-322 (1987).

233 14. Previdi, M. Radiative feedbacks on global precipitation. *Environ. Res. Lett.* **5**, 025211 (2010).

235 15. Yang, F., Kumar, A., Schlesinger, M. E. & Wang, W. Intensity of hydrological cycles in warmer climates. *J. Clim.* **16**, 2419-2423 (2003).

237   16. Dong, B., Gregory, J. M. & Sutton, R. T. Understanding land–sea warming contrast in

238   response to increasing greenhouse gases. Part I: Transient adjustment. *J. Clim.* **22**, 3079-3097

239   (2009).

240   17. Bony, S. et al. Robust direct effect of carbon dioxide on tropical circulation and regional

241   precipitation. *Nature Geosci.* **6**, 447-451 (2013).

242   18. Bala, G., Caldeira K. & Nemani, R. Fast versus slow response in climate change:

243   implications for the global hydrological cycle. *Clim. Dynam.* **35**, 423-434 (2010).

244   19. Andrews, T., Forster, P. M., Boucher, O., Bellouin, N. & Jones, A. Precipitation, radiative

245   forcing and global temperature change. *Geophys. Res. Lett.* **37**, L14701 (2010).

246   20. Gregory, J. M. *et al.* A new method for diagnosing radiative forcing and climate sensitivity.

247   *Geophys. Res. Lett.* **31**, L03205 (2004).

248   21. Wielicki, B. A. *et al.* Clouds and the Earth's Radiant Energy System (CERES): An Earth

249   observing system experiment. *Bull. Am. Meteorol. Soc.* **77**, 853-868 (1996).

250   22. Kato, S. *et al.* Surface irradiances consistent with CERES-derived top-of-atmosphere

251   shortwave and longwave irradiances. *J. Clim.* **26**, 2719-2740 (2013).

252   23. Collins, W. D. *et al.* Radiative forcing by well-mixed greenhouse gases: Estimates from

253   climate models in the Intergovernmental Panel on Climate Change (IPCC) Fourth

254   Assessment Report (AR4). *J. Geophys. Res.* **111**, D14317 (2006).

255   24. Oreopoulos, L. *et al.* The Continual Intercomparison of Radiation Codes: Results from Phase

256   I. *J. Geophys. Res.* **117**, D06118 (2012).

257   25. Pincus, R. *et al.* Radiative flux and forcing parameterization error in aerosol-free clear skies.

258   *Geophys. Res. Lett.* **42**, 5485-5492 (2015).

259   26. Mauritsen, T. & Stevens, B. Missing iris effect as a possible cause of muted hydrological

260   change and high climate sensitivity in models. *Nature Geosci.* **8**, 346-351 (2015).

261   27. Zhang, Y., Rossow, W. B., Lacis, A. A., Oinas V. & Mishchenko, M. I. Calculation of

262   radiative fluxes from the surface to top of atmosphere based on ISCCP and other global data

263   sets: Refinements of the radiative transfer model and the input data. *J. Geophys. Res.* **109**,

264   D19105 (2004).

265   28. Voldoire, A. *et al.* The CNRM-CM5.1 global climate model: description and basic

266   evaluation. *Clim. Dynam.* **40**, 2091-2121 (2013).

267   29. Taylor, K. E., Stouffer, R. J. & Meehl, G. A. An overview of CMIP5 and the experimental

268   design. *Bull. Am. Meteorol. Soc.* **93**, 485-498 (2012).

269

292   **Author Contributions**

293   A.M.D., X.Q., and A.H. designed the methodology. A.M.D. performed the analysis and wrote

294   the paper.   M.D.Z. provided the kernel-derived temperature-mediated shortwave absorption

295   response estimates. All authors discussed the results and edited the manuscript.

296

297   **Author Information**

298   The authors declare no competing financial interests. Correspondence and requests for materials

299   should be addressed to A.M.D. (adeangelis@ucla.edu).

300

301   **Figure Legends**

302

303   **Figure 1. The atmospheric energy budget.** (a) Schematic of the fluxes considered in the

304   budget.   All fluxes (arrows) shown in the schematic are defined positive; some represent

13

305   downward (denoted with subscript d) and others upward (denoted with subscript u) fluxes at the

306   top-of-atmosphere (TOA) or surface (SFC). All flux arrows are drawn with the same length for

307   simplicity. The four main energy budget terms considered in this study (Eq. 1) are identified

308   with blue text. Two of them are radiative and are derived from individual longwave (LW) or

309   shortwave (SW) flux components, following the equations in panel (a): net atmospheric

310   longwave cooling (LWC, the sum of upward LW flux at TOA and net downward LW flux at the

311   SFC) and shortwave absorption (SWA, net downward SW flux at TOA minus net downward SW

312   flux at the SFC). The other two are the latent heat release from precipitation (L_vP, latent heat of

313   vaporization multiplied by precipitation rate) and sensible heat flux from the surface to

314   atmosphere (SH). (b) The global-mean values of the four terms simulated by the CMIP5

315   ensemble for the pre-industrial control simulation (average over 150 years), Representative

316   Concentration Pathway scenario 8.5 (RCP8.5, average over 2091-2100), and abrupt quadrupled

317   CO_2 scenario (average for years 141-150 after CO_2 quadrupling in all models except

318   CNRM-CM5-2 and IPSL-CM5A-MR, where it is for years 131-140). The model mean is shown

319   in all cases, and the radiative terms are computed using all-sky fluxes. All terms are positive.

320

321   **Figure 2. Relationship between temperature-mediated L_vP and SWA responses.** (a) The

322   temperature-mediated responses of L_vP ($L_v dP/dT$) and SWA ($dSWA/dT$) for all-sky (indicated

323   with all-) and clear-sky (indicated with clr-) are shown. The values are computed using model-

324   produced fluxes (as in Extended Data Fig. 1) except in the case of clr-$dSWA/dT$(k), in which

325   they are computed with radiative kernels (Methods). Individual CMIP5 models are shown as

326   blue circles. The numbers above the abscissa are the cross-model correlations between

327    $L_v dP/dT$ and each $dSWA/dT$. The number in parentheses is the correlation between model-

14

328   produced and kernel-derived clear-sky $dSWA/dT$.   (b) Scatterplot of the model-produced

329      $L_v dP/dT$ vs. clear-sky $dSWA/dT$ for the 25 models. Note that the abscissa and ordinate axes

330   have the same scale. Model numbers are defined in Extended Data Table 1.

331

332   **Figure 3. The sensitivity of solar absorption to varying atmospheric water vapor.** (a)

333   Clear-sky *SWA* normalized by incoming solar flux versus column precipitable water (*PW*) in the

334   pre-industrial climate for selected models and for CERES-EBAF estimates with three *PW*

335   datasets (see Methods). The slope of the curve represents the sensitivity of *SWA* to varying *PW*

336   ($dSWA/dPW$) and its value is given in the legends for each model/dataset (%/[kg m^{-2}]). (b)

337   Scatterplot of the (clear-sky) temperature-mediated *SWA* response to CO_2 forcing, $dSWA/dT$

338   (Fig. 2b), versus $dSWA/dPW$ (panel a) for the 25 models. In (b), the width of the horizontal

339   shading for each model represents the 95% confidence interval (CI) of the regression slope to the

340   *SWA* versus *PW* curve (Methods). Statistical uncertainty of the CERES-EBAF $dSWA/dPW$

341   estimate combining all *PW* datasets is shown with vertical dashed lines (obs). It is computed by

342   (1) calculating the 95% CI of the slope of the CERES-EBAF curve with each individual *PW*

343   dataset, then (2) calculating the absolute minimum to maximum of the three CIs (i.e., the

344   minimum of the lower bounds of all CIs to the maximum of the upper bounds of all CIs).

345

346   **Figure 4. Shortwave parametrization schemes.** The relationship between $dSWA/dPW$ (Fig. 3)

347   and characteristics of the parameterization scheme for solar absorption by water vapor in a

348   cloud-free atmosphere, with colors for each model referring to different types of

349   parameterizations as described in the legend (*N* refers to the number of exponential terms

350   representing water vapor absorption). References and further discussion are given in Extended

351 Data Table 1 and Methods, respectively. Model numbers are identified. The width of horizontal

352 shading for models and the vertical dashed lines for observations (obs) represent statistical

353 uncertainties of $dSWA/dPW$, as described in Fig. 3. The 95% CI for an estimate of

354 $dSWA/dPW$ based on ISCCP-FD (Methods) is also shown with vertical dashed lines.

355

356 **Methods**

357

358 **CMIP5 models.** The CMIP5 models[29] analyzed here are listed in Extended Data Table 1, with

359 corresponding references. We use one ensemble member (r1i1p1) from 25 models that had

360 available monthly output of atmospheric temperature and humidity, precipitation, and energy

361 fluxes for the pre-industrial control (piControl) and abrupt quadrupled CO_2 (abrupt4xCO_2)

362 experiments at the time of analysis.

363

364 **Temperature-mediated responses and rapid adjustments.** The Gregory method[10,20] is

365 employed using each model's piControl and abrupt4xCO_2 run. For each year of the

366 abrupt4xCO_2 run, the global-mean abrupt4xCO_2 anomaly of a physical quantity (e.g., L_vP)

367 relative to the piControl simulation is paired against the corresponding anomaly of 2-m air

368 temperature, generating a scatterplot (Extended Data Fig. 1). To compute the annual anomalies,

369 the piControl 21-year mean, centered on the corresponding year of the abrupt4xCO_2 simulation,

370 is subtracted from each abrupt4xCO_2 1-year mean. Subtracting this running mean removes

371 possible influences of climate model drift on the anomalies. The scatterplots are generated using

372 150 years of the abrupt4xCO_2 simulation when available (140 years are available from the

373 CNRM-CM-2 and IPSL-CM5A-MR models). A least-squares linear regression is then applied

374　to each scatterplot, with the slope and y-intercept of the fit representing the temperature-

375　mediated and rapid responses to CO_2 forcing, respectively.

376　　　The Gregory methodology is displayed visually for the GFDL-CM3 model in Extended

377　Data Fig. 1. It shows the yearly evolution of globally-averaged *LWC*, *SWA*, *SH*, and L_vP changes

378　after a quadrupling of atmospheric CO_2. The physical interpretation of these changes has been

379　thoroughly discussed in numerous studies[6,12,16,18,30-32]. The high degree of linearity of the

380　scatterplots demonstrates the reliability of this approach for separating temperature-mediated

381　responses and rapid adjustments.

382　　　As shown in Fig. 2, model spread in the temperature-mediated *SWA* response,

383　$dSWA/dT$, particularly for clear-sky, substantially contributes to the spread in $L_v dP/dT$. The

384　*total* change in L_vP per unit warming ($L_v\Delta P/\Delta T$, which includes the temperature-mediated

385　response and rapid adjustment), however, is not correlated with the corresponding total change in

386　*SWA* across models (Extended Data Fig. 3a). This may be the consequence of large scatter in the

387　rapid adjustment of L_vP, which is not strongly related to that of *SWA* (Extended Data Fig. 3b).

388　Ref. [7] found the opposite result using 8 CMIP3 models: that the temperature-mediated

389　responses of latent heating and solar absorption are not correlated, but that total changes at a

390　warming of 2 K are anti-correlated (r= -0.66). The differences between their results and ours

391　likely originates from different analysis methods and sampling. For one, they use only 8 models

392　from CMIP3 while we use 25 from CMIP5. Additionally, they combine different types of CO_2

393　forcing scenarios (e.g., 1% increase to CO_2 doubling or quadrupling and instantaneous CO_2

394　doubling) and base their temperature-mediated estimates on scatterplots of relatively few (5-10)

395　data points from each simulation. It is shown in their analysis that quite different slopes may be

396　obtained from different forcing simulations even with the same model. We argue that our results

397   are more robust. In addition to using many more models, we base our temperature-mediated

398   estimates on a large number of data points (140-150) from a single forcing scenario

399   (instantaneous CO_2 quadrupling). Furthermore, our findings are consistent with ref. [4] who also

400   found that *total* changes in precipitation (per unit warming) are not correlated with those in

401   shortwave absorption under doubled CO_2 using a larger sample of CMIP3 models (14) than ref.

402   [7].

403

404   **Radiative kernels and water vapor responses.** Radiative kernels were developed using an

405   offline version of the MPI-ECHAM5 radiation code and represent the sensitivity of top-of-

406   atmosphere (TOA) and surface shortwave radiative fluxes to small perturbations in atmospheric

407   specific humidity and surface albedo[14]. Global-mean temperature-mediated *SWA* responses due

408   to water vapor changes are computed as follows: 1) Temperature-mediated responses in the

409   logarithm of specific humidity at all months, locations, and pressure levels are multiplied by the

410   shortwave specific humidity atmospheric (TOA minus surface) kernel for clear-sky. Global-

411   annual-mean kernel values are shown in Extended Data Fig. 4a. Specific humidity responses are

412   computed as the difference in abrupt4xCO_2-piControl anomalies averaged over years 121-150

413   and 1-30 of the abrupt4xCO_2 simulation, normalized by the corresponding difference in 2-m air

414   temperature. 2) The product is integrated over the depth of the troposphere (defined as all levels

415   between the surface and a tropopause height that varies linearly with latitude from 100 hPa on

416   the Equator to 300 hPa at the poles), and then averaged over all months and locations.

417   Temperature-mediated *SWA* responses due to surface albedo are computed in similar fashion but

418   with surface albedo kernels and temperature-mediated responses. The final kernel-derived

419   temperature-mediated *SWA* response for each model [$dSWA/dT$(k) in Fig. 2a] is the sum of the

420   water vapor and surface albedo components of the response, with the vapor component

421   dominating[14].

422   It should be noted that the computation of atmospheric radiative feedbacks using kernels

423   is associated with uncertainty[12,14]. In this study, our goal is not to obtain perfectly accurate

424   quantitative estimates of temperature-mediated responses with the kernels. Rather, we apply the

425   kernels to assess whether model spread in $dSWA/dT$ originates from differences in the response

426   of atmospheric water vapor to surface warming. We argue that the kernel calculations are

427   sufficiently accurate for this purpose. Extended Data Fig. 4 shows that kernel-derived

428    $dSWA/dT$ is significantly correlated across models with globally-averaged responses of water

429   vapor, as expected. By contrast, actual model-produced $dSWA/dT$ is not correlated with the

430   water vapor responses, supporting that spread in $dSWA/dT$ is not explained by differences in the

431   water vapor response. This may be partly because water vapor responses (in fractional sense)

432   and their intermodel variability are largest in the upper troposphere, where water vapor changes

433   have little effect on total-column SWA (Extended Data Fig. 4a). Our conclusions are also

434   supported by ref. [12], where it is independently shown that CMIP5 spread in enhanced solar

435   absorption under CO_2 forcing cannot be reproduced by imposing simulated changes in

436   atmospheric temperature and moisture on the single-column Fu-Liou radiative transfer model.

437   Nonetheless, to assess uncertainty in kernel-estimated temperature-mediated responses,

438   calculations with additional kernels produced from different radiation codes would be necessary.

439

440   **The sensitivity of *SWA* to a unit water vapor change.** *SWA* sensitivity to water vapor

441   variability is computed based on spatial and temporal variations of *PW* in the control climate.

442   All grid cells and months from 150 years of a model's piControl simulation over the tropical

443   oceans are aggregated into one sample to compute the sensitivity. The years 2001-2009 and

444   1984-2009 are used for estimates based on CERES-EBAF and ISCCP-FD, respectively.

445   Tropical oceans are defined as grid cells with centers between 30°S and 30°N and with land

446   fraction less than 0.50. All model output is regridded to 2.5° x 2.5° lat-lon prior to performing

447   calculations. To compute the sensitivity, the clear-sky *SWA* at each grid cell and for each month

448   is normalized by incoming solar radiation, then binned according to *PW* with equal bin size of

449   2 kg m^{-2}. *SWA* is averaged within each *PW* bin and plotted against the bin center value (Fig. 3a).

450   Only bins with at least 20 data values in every model and observational source are considered,

451   resulting in a common *PW* range of 12-58 kg m^{-2}. The linear regression slope of the *SWA* versus

452   *PW* scatterplot represents the *SWA* sensitivity to varying *PW* (i.e., $dSWA/dPW$). Statistical

453   uncertainty in $dSWA/dPW$ is computed as the 95% confidence interval of the regression slope,

454   derived from the estimated standard error of the slope parameter[33].

455   We consider only tropical oceans when computing $dSWA/dPW$ due to the relatively

456   small variability of surface albedo and solar zenith angle within this region, better isolating the

457   effect of *PW* on *SWA*. To examine whether the remaining small variations of surface albedo or

458   solar zenith angle affect $dSWA/dPW$, we re-compute $dSWA/dPW$ by also conditioning on

459   surface albedo and/or zenith angle. Specifically, $dSWA/dPW$ is recomputed from locations and

460   months where albedo and/or zenith angle vary by no more than 0.01 or 1°, respectively. While

461   the recomputed $dSWA/dPW$ values vary slightly from the original values computed with the

462   entire domain, they are highly correlated with the original values across models (not shown).

463   This suggests the influence of albedo and zenith angle on $dSWA/dPW$ is very small.

464   Our computation of $dSWA/dPW$ does not isolate the effect of aerosols on *SWA*. Models

465   differ in the types of aerosols represented, the concentrations and optical properties of the

466   aerosols, and the quantitative parameterization of aerosol scattering and absorption.   These

467   factors could potentially modulate the relationship between *SWA* and *PW* in models, and thus

468    $dSWA/dPW$ may not completely reflect the physics of water vapor absorption.   One possible

469   example of this is with the GFDL models.   All three GFDL models (GFDL-CM3, GFDL-

470   ESM2G, GFDL-ESM2M) use the same shortwave parameterization for water vapor absorption

471   and scattering by aerosols[34-37]; yet the CM3 absorbs more solar radiation in moist conditions,

472   leading to larger $dSWA/dPW$ (Extended Data Fig. 5).   The CM3 implements an interactive

473   aerosol scheme with different aerosol optical properties than the ESM models (which prescribe

474   aerosols), resulting in enhanced and more realistic downward clear-sky surface shortwave flux

475   due to reduced aerosol direct effects[34].   We speculate that the reduced aerosol direct effects may

476   lead to more solar radiation available for absorption by lower tropospheric water vapor, and thus

477   larger *SWA* in moist conditions in the CM3.   The extent that differences in aerosol

478   concentrations/properties affect the variability in $dSWA/dPW$ among other models is unknown

479   without a more rigorous and controlled investigation.   However, we suspect these effects are

480   generally small, as 1) the GFDL models represent the only instance in which $dSWA/dPW$

481   significantly differs among models with similar parameterizations of solar absorption by water

482   vapor (Fig. 4, Extended Data Fig. 6), and 2) $dSWA/dPW$ computed using different forcing

483   scenarios (e.g., historical and RCP8.5, which potentially exhibit large variability in aerosols) are

484   very similar to those computed with the piControl (not shown).

485   Stratospheric ozone is another strong absorber of solar radiation.   Ozone may influence

486    $dSWA/dPW$ if its concentration varies systematically with atmospheric moisture.   Although

487   column-integrated ozone tends to decrease with increasing *PW* in 16 models that have available

488   ozone output, there is no cross-model correlation between the sensitivity of ozone concentration

489   to varying *PW* and $dSWA/dPW$ (not shown). This suggests the covariability of ozone and *PW*

490   does not systematically affect $dSWA/dPW$. Furthermore, $dSWA/dPW$ is similar to that in

491   Extended Data Fig. 5 when it is computed from a smaller sample of locations and months

492   exhibiting little variability in column-integrated ozone (not shown). This strengthens the case

493   that ozone is not significantly affecting model variability in $dSWA/dPW$. However, the

494   parameterization of ozone absorption likely influences the mean position of the *SWA* versus *PW*

495   curve for each model (i.e., average *SWA* over the range of *PW* analyzed). One possible example

496   of this is with the INM-CM4 and MRI-CGCM3 models. Both models use the same shortwave

497   parameterization for water vapor absorption[38], but have different treatments of solar absorption

498   by ozone[39,40]. We speculate that this partly explains the similar slopes but different vertical

499   placement of the *SWA* versus *PW* curves for these models (Extended Data Fig. 5).

500   As discussed above, $dSWA/dPW$ values are nearly invariant to the simulation (e.g.

501   piControl, abrupt4xCO2, historical, RCP8.5) from which they are calculated in models (not

502   shown). They are also very similar when computed from a subset of years as short as that used

503   from observations (2001-2009). Furthermore, $dSWA/dPW$ computed from various percentiles

504   of the *SWA* distribution within each *PW* bin (ranging from the 10th to 90th percentile) are similar

505   to those computed with the *SWA* bin mean (not shown). These findings further demonstrate that

506   the methodology robustly quantifies the dependency of *SWA* on atmospheric moisture.

507

508   **Observations.** The CERES-EBAF dataset provides clear-sky radiative fluxes at the TOA and

509   surface on a grid comparable to climate models and has global coverage. TOA fluxes are based

510   on satellite measurements, and surface fluxes are generated with a radiative transfer model

511   constrained by the TOA fluxes[22]. Although the surface fluxes are model produced, they are

512 computed with a radiative transfer algorithm that is arguably more advanced and physically-

513 based than that used in most climate models. In particular, the radiation code for solar

514 absorption employs the formal correlated-k-distribution framework with absorption coefficients

515 (k-values) being determined directly from detailed line-by-line (LBL)-generated k-

516 distributions[41,42]. This approach is arguably superior to that in most CMIP5 models, in which k-

517 values are in many cases determined with non-physical mathematical optimization procedures

518 (e.g., refs. [36] and [43]). In addition, the treatment of pressure-temperature-concentration

519 dependence of k-values in the CERES-EBAF scheme is more physical and higher in resolution

520 than most CMIP5 models[41]. The final parameterization describing water vapor absorption in

521 CERES-EBAF also has many mathematical terms (>50) approximating shortwave

522 transmission[44]. CERES-EBAF surface fluxes are in good agreement with point observations[22]

523 and the radiation scheme used to generate surface fluxes performs well when compared with

524 recent LBL calculations[24].

525   To compute CERES-EBAF-derived $dSWA/dPW$, water vapor data is taken from three

526 sources: 1) the Special Sensor Microwave Imager (SSM/I)[45]; 2) a product developed by Remote

527 Sensing Systems (RSS) that combines measurements from various instruments, including SSM/I,

528 the Special Sensor Microwave Imager Sounder (SSMIS), the Advanced Microwave Scanning

529 Radiometer (AMSR-E), and the WindSat Polarimetric Radiometer[46]; 3) the Television Infrared

530 Observation Satellite Operational Vertical Sounder (TOVS)[47]. ISCCP-FD-derived $dSWA/dPW$

531 is based on TOVS water vapor, which was used in development of the flux dataset[27].

532   The uncertainty range of CERES-EBAF-derived $dSWA/dPW$ shown in the figures (e.g.,

533 Figs. 3-4) reflects statistical uncertainty in the computation of $dSWA/dPW$ and uncertainty due

534 to the use of different PW datasets (see Fig. 3 caption). Inherent uncertainties in CERES-EBAF

535   fluxes, including possible measurement uncertainty, errors in the radiative transfer scheme, and

536   uncertainty in the methodology that generates clear-sky fluxes[22], are difficult to quantify and are

537   not included. Potential uncertainty in the individual PW measurements are also not accounted

538   for. Thus, the effective uncertainty of observed $dSWA/dPW$ is likely larger than indicated in the

539   figures. Nonetheless, the conclusion that most CMIP5 models underestimate $dSWA/dPW$ is

540   robust, as it is strongly supported by a recent study in which radiation schemes are evaluated

541   against high quality LBL calculations[25].

542

543   **Additional discussion of shortwave radiative transfer schemes.** The severe underestimation

544   of $dSWA/dPW$ by the GISS models stands out in Fig. 4. In these models, solar absorption by

545   water vapor is parameterized with a pseudo-k-distribution approach consisting of 15

546   mathematical terms[48-52]. Some of the other CMIP5 models in our analysis, including those with

547   the largest $dSWA/dPW$, use as many terms in their parameterizations (Fig. 4). Thus the poor

548   performance of the GISS parameterization is not simply the result of the number of computations

549   employed to approximate shortwave transmission.   Rather, the finer details of how the

550   parameters of the analytical expressions (e.g., pseudo absorption coefficients and weights for

551   terms) are developed and the quality of the reference calculations from which the

552   parameterizations were originally based, are probably important, among other characteristics.

553   The GISS parameterization employed in CMIP5 was developed from a combination of old and

554   relatively new methods[50-52].   The resulting analytical expressions, which combine pressure-

555   temperature-spectral absorption dependency, are known to underestimate solar absorption in

556   moist atmospheres based on comparison with modern LBL calculations[24,25]. Updates were made

557   to the GISS radiation scheme since CMIP5, and these will likely result in significant

558   improvements in solar absorption and $dSWA/dPW$ in future generations of the GISS model[25].

559   Aside from the GISS models, the number of mathematical terms employed in shortwave

560   parameterizations appear to exert a general influence on parameterization performance (Fig. 3c).

561   A specific example is with models developed at IPSL and CNRM. In these models, water vapor

562   absorption is parameterized with an algorithm originally developed in 1980 and later modified

563   for use in the operational European Center for Medium Range Weather Forecasts (ECMWF)

564   model[53,54]. It consists of a few shortwave bands, within which Padé Approximants represent

565   gaseous absorption by water vapor[53]. In the IPSL models, only two shortwave bands are used[54].

566   These models clearly underestimate mean SWA over the range of PW analyzed and $dSWA/dPW$

567   is smaller than that of all models except GISS (Extended Data Fig. 5). By contrast, the CNRM

568   scheme employs 6 total shortwave bands[28]. Mean SWA is considerably larger and more realistic

569   in these models compared to IPSL and $dSWA/dPW$ is marginally improved as well (Extended

570   Data Fig. 5). Thus the number of spectral bands and corresponding computations can have a

571   large impact on the realism of solar absorption.

572   A comparison of the models that implement a 7-band parameterization originally

573   developed by ref. [38] (BCC-CSM1.1, BCC-CSM1.1(m), CCSM4, INM-CM4, MRI-CGCM3,

574   NorESM1-M) sheds light on specific characteristics of parameterizations of gaseous absorption,

575   other than number of mathematical terms, that appear important for SWA. The original

576   parameterization for water vapor absorption by ref. [38] consists of a 7-term pseudo-k-

577   distribution summation with absorption coefficients and weights determined by fits to empirical

578   and LBL calculations, respectively[38,50]. It is employed by the INM-CM4 and MRI-CGCM3

579   models (Extended Data Fig. 6). The parameterization was later modified to account for

580 additional near-infrared water vapor absorption based on updated spectroscopic data and

581 continuum absorption in the shortwave, which resulted in refitting the 7 parameterized

582 absorption coefficients[55]. The updated parameterization is employed in the BCC-CSM1.1, BCC-

583 CSM1.1(m), CCSM4, and NorESM1-M models. The models using the updated parameterization

584 exhibit improved $dSWA/dPW$ by a small but non-negligible amount (Extended Data Fig. 6).

585 Consideration of weak water vapor absorption lines and continuum absorption are therefore

586 somewhat important for accurate simulation of changes in solar absorption in a warming climate.

587 This is consistent with the findings presented in refs. [55] and [56]. Note that most models with

588 larger and more realistic $dSWA/dPW$ tend to account for continuum absorption in their

589 parameterizations (Extended Data Fig. 6).

590   Other details of the CMIP5 shortwave parameterization schemes, including the treatment

591 of scattering by aerosols and molecules and of overlapping absorption by multiple gaseous

592 species, have not been thoroughly investigated here. They too may influence the intermodel

593 spread in $dSWA/dPW$. Even if these details are indeed influencing $dSWA/dPW$, it would not

594 change the conclusion that shortwave parameterizations *in general* are important for the spread

595 in simulated hydrologic cycle intensification.

596

597 **Constraining late 21st century precipitation changes.** We exploit the strong model

598 relationships among *SWA* and L_vP under CO_2 forcing (Extended Data Figs. 7a-b) to compute a

599 hypothetical change in L_vP that may occur at the end of the 21st century under realistic climate

600 forcing if the true temperature-mediated *SWA* response to CO_2 forcing, $dSWA/dT$, were

601 perfectly known. The "true" $dSWA/dT$ is approximated from the model relationship between

602 $dSWA/dT$ and $dSWA/dPW$, using the observed value of $dSWA/dPW$ based on CERES-EBAF

603   (Extended Data Fig. 7a). The resulting true value of $dSWA/dT$ is then used with the model

604   relationship between the temperature-mediated L_vP response, $L_v dP/dT$, and $dSWA/dT$ to

605   estimate a "bias" in $L_v dP/dT$ that originates from a bias in $dSWA/dT$ (Extended Data Fig. 7b).

606   The bias for each model is then removed from the predicted precipitation change at the end of

607   the 21st century in the RCP8.5 scenario relative to the piControl according to:

608    $$\frac{L_v \Delta P}{\Delta T}_{cons} = \frac{L_v \Delta P_{RCP8.5} - bias * \Delta T_{RCP8.5}}{\Delta T_{RCP8.5}} \tag{2}$$

609   where $\frac{L_v \Delta P}{\Delta T}_{cons}$ is the constrained total change in L_vP normalized by surface warming with the

610   bias removed, $L_v \Delta P_{RCP8.5}$ is the total late 21st century L_vP change (mean of years 2081-2100 in

611   RCP8.5 minus mean of years 131-150 in piControl), and $\Delta T_{RCP8.5}$ is the late 21st century 2-m air

612   temperature change computed similarly to $L_v \Delta P_{RCP8.5}$.

613   The above procedure makes several assumptions, including: 1) the middle of the range in

614   CERES-EBAF-computed $dSWA/dPW$ is most representative of the real atmosphere, 2) the best

615   "true" value of $dSWA/dT$ (Extended Data Fig. 7a, blue star) and $L_v dP/dT$ (Extended Data Fig.

616   7b, black horizontal line) occurs at the linear regression line on the cross-model scatterplots, and

617   3) $L_v dP/dT$ contributes linearly (with ΔT) to the total late 21st century change in L_vP computed

618   from RCP8.5, as depicted in Equation 2.

619   Removing the bias in $L_v dP/dT$ due to a bias in $dSWA/dT$ reduces the model spread in

620   predicted precipitation change per unit warming at the end of the 21st century by 37%, and

621   reduces the ensemble mean increase by 38% (Extended Data Fig. 7c). Even if we do not

622   normalize by differences in surface warming ΔT, which is the main driver of the spread in total

623   precipitation change $L_v \Delta P$, a discernible reduction in spread by 27% and ensemble mean

624   increase by 25% can be achieved (Extended Data Fig. 7d). The spread reduction is substantial

625   considering the numerous factors in addition to the temperature-mediated *SWA* response to CO_2

626   forcing potentially contributing to model scatter in RCP8.5 projections.   These include

627   temperature-mediated responses of other energy budget components (Extended Data Fig. 2),

628   greenhouse gas forcing other than CO_2, aerosols, and the rapid L_vP adjustments to all forcings.

629   For instance, ref. [4] demonstrated the potent role of black carbon forcing for CMIP3 spread in

630   simulated global precipitation change under a realistic climate change scenario. That we obtain a

631   37% reduction in $L_v\Delta P/\Delta T$ under RCP8.5 by only constraining the temperature-mediated

632   component of *SWA* change under pure CO_2 forcing (and only a somewhat larger reduction by

633   45% when repeating the same exercise with the quadrupled CO_2 runs, not shown) suggests that

634   the role of black carbon forcing on the spread may be less potent in CMIP5 than CMIP3. This is

635   an interesting possibility worthy of further analysis.

636   How may uncertainty in late 21st century precipitation change be reduced further? As

637   discussed above, a realistic climate change scenario includes greenhouse gas forcing (from CO_2

638   and other gases), aerosol forcing, and rapid adjustments to these forcings.   A better

639   understanding of all these factors is therefore critical, including of the rapid adjustment to CO_2

640   forcing. This factor has a non-negligible spread (Extended Data Fig. 3b) and is not strongly

641   correlated with the corresponding intermodel variations in temperature-mediated response

642   (r= -0.23, not shown). Additionally, the spread in the temperature-mediated L_vP response to CO_2

643   forcing is not only driven by the *SWA* component, as indicated by residual scatter in Fig. 2b.

644   Extended Data Fig. 2 shows that the net atmospheric longwave cooling response, $dLWC/dT$,

645   also has a large spread that is correlated with L_vdP/dT. $dSWA/dT$ and $dLWC/dT$ are not

646   correlated with each other (|r|<0.1, not shown), suggesting that $dLWC/dT$ is another independent

647   source of spread that demands better understanding. $dLWC/dT$ is only correlated with

648 $L_v dP/dT$ for all-sky (Extended Data Fig. 2), implying that clouds may play an important role in

649 the intermodel relationship. This is different from the case of $dSWA/dT$, in which clear-sky

650 absorption by water vapor is critical.

651

652 **Code Availability.** Any codes used in the analysis in this paper and in the production of figures

653 can be made available upon request. Please contact adeangelis@ucla.edu.

654

655 **Methods/Extended Data References**

656

657 30. Andrews, T., Forster, P. M. & Gregory, J. M. A surface energy perspective on climate

658   change. *J. Clim.* **22**, 2557-2570 (2009).

659 31. Lu, J. & Cai, M. Stabilization of the atmospheric boundary layer and the muted global

660   hydrological cycle response to global warming. *J. Hydromet.* **10**, 347-352 (2009).

661 32. Allan, R. P. et al. Physically consistent responses of the global atmospheric hydrological

662   cycle in models and observations. *Surv. Geophys.* **35**, 533-552 (2014).

663 33. Devore, J. L. Simple linear regression and correlation. In *Probability and Statistics for*

664   *Engineering and the Sciences* Edn. 7 (eds. Crockett, C., Gershman, B. & Broyer, R.) 12.446-

665   12.499 (Duxbury Press, Belmont, CA, USA, 2008).

666 34. Donner, L. J. *et al.* The dynamical core, physical parameterizations, and basic simulation

667   characteristics of the atmospheric component AM3 of the GFDL global coupled model CM3.

668   *J. Clim.* **24**, 3484-3519 (2011).

669   35. Dunne, J. P. *et al.* GFDL's ESM2 global coupled climate–carbon Earth system models. Part

670   I: Physical formulation and baseline simulation characteristics. *J. Clim.* **25**, 6646-6665

671   (2012).

672   36. Freidenreich, S. M. & Ramaswamy, V. A new multiple-band solar radiative parameterization

673   for general circulation models. *J. Geophys. Res.* **104**, 31389-31409 (1999).

674   37. Anderson, J. L. *et al.* The new GFDL global atmosphere and land model AM2–LM2:

675   Evaluation with prescribed SST simulations. *J. Clim.* **17**, 4641-4673 (2004).

676   38. Briegleb, B. P. Delta-eddington approximation for solar radiation in the NCAR Community

677   Climate Model. *J. Geophys. Res.* **97**, D7, 7603-7612 (1992).

678   39. Galin, V. Y. Parametrization of radiative processes in the DNM atmospheric model. *Izv.,*

679   *Atmos. Ocean. Phys.* **34**, 339-347 (1998).

680   40. Yukimoto, S. *et al.* Meteorological Research Institute-Earth System Model Version 1 (MRI-

681   ESM1) -Model description-. Tech. Rep. of the Meteorological Research Institute No. 64

682   (Meteorological Research Institute, Tsukuba-city, Ibaraki, Japan, 2011).

683   41. Kato, S., Ackerman, T. P., Mather, J. H. & Clothiaux, E. E. The k-distribution method and

684   correlated-k approximation for a shortwave radiative transfer model. *J. Quant. Spect. Rad.*

685   *Trans.* **62**, 109-121 (1999).

686   42. Kato, S. *et al.* Improvements of top-of-atmosphere and surface irradiance computations with

687   CALIPSO-, CloudSat-, and MODIS- derived cloud and aerosol properties. *J. Geophys. Res.*

688   **116**, D19209 (2011).

689   43. Sekiguchi, M. & Nakajima, T. A k-distribution-based radiation code and its computational

690   optimization for an atmospheric general circulation model. *J. Quant. Spect. Rad. Trans.* **109**,

691   2779-2793 (2008).

692   44. Rose, F. *et al.* CERES Proto-Edition 3 radiative transfer: Tests and radiative closure over

693   surface validation sites, in *12th Conference on Atmospheric Radiation* (American

694   Meteorological Society, Madison, WI, 10-14 July 2006). [Available at

695   https://ams.confex.com/ams/pdfpapers/112358.pdf]

696   45. Ferraro, R. R., Weng, F., Grody, N. C. & Basist, A. An eight-year (1987–1994) time series of

697   rainfall, clouds, water vapor, snow cover, and sea ice derived from SSM/I measurements.

698   *Bull. Am. Meteorol. Soc.* **77**, 891–905 (1996).

699   46. Remote Sensing Systems, 2012, updated July 2014. Monthly Mean Total Precipitable Water

700   Data Set on a 1 degree grid made from Remote Sensing Systems Version-7 Microwave

701   Radiometer Data, accessed August 2014. Santa Rosa, CA, USA. Available at

702   www.remss.com.

703   47. Kidwell, K. NOAA Polar Orbiter Data Products Users Guide, 304 pp., National

704   Environmental Satellite Data and Information Service, Silver Spring, MD (1995).

705   48. Schmidt, G. A. *et al.* Present-day atmospheric simulations using GISS ModelE: Comparison

706   to in situ, satellite, and reanalysis data. *J. Clim.* **19**, 153-192 (2006).

707   49. Schmidt, G. A. *et al.* Configuration and assessment of the GISS ModelE2 contributions to the

708   CMIP5 archive. *J. Adv. Model. Earth Syst.* **6**, 141-184 (2014).

709   50. Lacis, A. A. & Hansen, J. E. A parameterization for the absorption of solar radiation in the

710   Earth's atmosphere. *J. Atmos. Sci.* **31**, 118-133 (1974).

711   51. Hansen, J. *et al.* Efficient three-dimensional global models for climate studies: Models I and

712   II. *Mon. Wea. Rev.* **111**, 609-662 (1983).

713   52. Lacis, A. A. & Oinas V. A description of the correlated k distribution method for modeling

714   nongray gaseous absorption, thermal emission, and multiple scattering in vertically

715   inhomogeneous atmospheres. *J. Geophys. Res.* **96**, D5, 9027-9063 (1991).

716   53. Fouquart, Y. & Bonnel, B. Computations of solar heating of the Earth's atmosphere: A new

717   parameterization. *Contrib. Atmos. Phys.* **53**, 35-62 (1980).

718   54. Morcrette, J.-J. Radiation and cloud radiative properties in the European Centre for Medium

719   Range Weather Forecasts forecasting system. *J. Geophys. Res.* **96**, D5, 9121-9132 (1991).

720   55. Collins, W. D., Lee-Taylor, J. M., Edwards, D. P. & Francis, G. L. Effects of increased near-

721   infrared absorption by water vapor on the climate system. *J. Geophys. Res.* **111**, D18109

722   (2006).

723   56. Paynter, D. & Ramaswamy, V. Investigating the impact of the shortwave water vapor

724   continuum upon climate simulations using GFDL global models. *J. Geophys. Res. Atmos.*

725   **119**, 10720-10737 (2014).

726   57. Hewitt, H. T. *et al.* Design and implementation of the infrastructure of HadGEM3: the next-

727   generation Met Office climate modelling system. *Geosci. Model Dev.* **4**, 223-253 (2011).

728   58. Bi, D. *et al.* The ACCESS coupled model: description, control climate and evaluation. *Aust.*

729   *Meteorol. Oceanog. J.* **63**, 41-64 (2013).

730   59. Edwards, J. M. & Slingo, A. Studies with a flexible new radiation code. I: Choosing a

731   configuration for a large-scale model. *Q. J. R. Meteorol. Soc.* **122**, 689-719 (1996).

732   60. Cusack, S., Edwards, J. M. & Crowther, J. M. Investigating k distribution methods for

733   parameterizing gaseous absorption in the Hadley Centre climate model. *J. Geophys. Res.*

734   **104**, 2051-2057 (1999).

735   61. Wu, T. *et al.* The Beijing Climate Center atmospheric general circulation model: description

736   and its performance for the present-day climate. *Clim. Dynam.* **34**, 123-147 (2010).

737   62. Collins, W. D. *et al.* Description of the NCAR Community Atmosphere Model (CAM 3.0).

738   Tech. Rep. NCAR/TN-464+STR (National Center for Atmospheric Research, Boulder,

739   Colorado, 2004).

740   63. Chylek, P., Li, J., Dubey, M. K., Wang, M. & Lesins, G. Observed and model simulated 20th

741   century Arctic temperature variability: Canadian Earth System Model CanESM2. *Atmos.*

742   *Chem. Phys. Discuss.* **11**, 22893-22907 (2011).

743   64. Li, J. & Barker, H. W. A radiation algorithm with correlated-k distribution. Part I: Local

744   thermal equilibrium. *J. Atmos. Sci.* **62**, 286-309 (2005).

745   65. Gent, P. R. *et al.* The Community Climate System Model Version 4. *J. Clim.* **24**, 4973-4991

746   (2011).

747   66. Neale, R. B. *et al.* Description of the NCAR Community Atmosphere Model (CAM 4.0).

748   Tech. Rep. NCAR/TN-485+STR (National Center for Atmospheric Research, Boulder,

749   Colorado, 2010).

750   67. Martin, G. M. *et al.* The physical properties of the atmosphere in the new Hadley Centre

751   Global Environmental Model (HadGEM1). Part I: Model description and global climatology.

752   *J. Clim.* **19**, 1274-1301 (2006).

753   68. Collins, W. J. *et al.* Development and evaluation of an Earth-System model – HadGEM2.

754   *Geosci. Model Dev.* **4**, 1051-1075 (2011).

755   69. Volodin, E. M., Dianskii, N. A. & Gusev, A. V. Simulating present day climate with the

756   INMCM4.0 coupled model of the atmospheric and oceanic general circulations. *Izv., Atmos.*

757   *Ocean. Phys.* **46**, 414-431 (2010).

33

758   70. Dufresne, J.-L. *et al.* Climate change projections using the IPSL-CM5 Earth System Model:

759   from CMIP3 to CMIP5. *Clim. Dynam.* **40**, 2123-2165 (2013).

760   71. Hourdin, F. *et al.* LMDZ5B: the atmospheric component of the IPSL climate model with

761   revisited parameterizations for clouds and convection. *Clim. Dynam.* **40**, 2193-2222 (2013).

762   72. Watanabe, S. *et al.* MIROC-ESM 2010: model description and basic results of CMIP5-

763   20c3m experiments. *Geosci. Model Dev.* **4**, 845-872 (2011).

764   73. Watanabe, M. *et al.* Improved climate simulation by MIROC5: mean states, variability, and

765   climate sensitivity. *J. Clim.* **23**, 6312-6335 (2010).

766   74. Jungclaus, J. H. *et al.* Characteristics of the ocean simulations in the Max Planck Institute

767   Ocean Model (MPIOM) the ocean component of the MPI-Earth system model. *J. Adv.*

768   *Model. Earth Syst.* **5**, 422-446 (2013).

769   75. Stevens, B. *et al.* Atmospheric component of the MPI-M Earth system model: ECHAM6. *J.*

770   *Adv. Model. Earth Syst.* **5**, 146-172 (2013).

771   76. Mlawer, E. J., Taubman, S. J., Brown, P. D., Iacono, M. J. & Clough, S. A. Radiative transfer

772   for inhomogeneous atmospheres: RRTM, a validated correlated-k model for the longwave. *J.*

773   *Geophys. Res.* **102**, D14, 16663-16682 (1997).

774   77. Mlawer, E. J. & Clough, S. A. On the extension of rapid radiative transfer model to the

775   shortwave region, in *Proceedings of the 6th Atmospheric Radiation Measurement Science*

776   *Team Meeting* (U.S. Department of Energy, CONF-9603149, 1997).

777   78. Iacono, M. J. *et al.* Radiative forcing by long-lived greenhouse gases: Calculations with the

778   AER radiative transfer models. *J. Geophys. Res.* **113**, D13103 (2008).

779   79. Yukimoto, S. *et al.* A new global climate model of the Meteorological Research Institute:

780   MRI-CGCM3. *J. Meteorol. Soc. Jap.* **90A**, 23-64 (2012).

781   80. Bentsen, M. *et al.* The Norwegian Earth System Model, NorESM1-M – Part 1: Description

782   and basic evaluation of the physical climate. *Geosci. Model Dev.* **6**, 687-720 (2013).

783

784   **Extended Data Legends**

785

786   **Extended Data Table 1. CMIP5 models analyzed in this paper.** The numbers used to identify

787   models throughout the paper are given in the first column. General references and references

788   documenting the details of the shortwave parameterization schemes, particularly with regard to

789   the treatment of gaseous absorption, are listed in the rightmost columns. Additional information

790   about the BCC-CSM1.1 models may be found at the webpage given under the modeling

791   institution.

792

793   **Extended Data Figure 1. Demonstration of the Gregory method for the GFDL-CM3.**

794   Global-annual-mean anomalies (abrupt4xCO$_2$-piControl) in atmospheric energy budget terms

795   (latent heat release from precipitation [L_vP], net longwave cooling [LWC], shortwave absorption

796   [SWA], and sensible heating [SH]) are regressed against those in 2-m air temperature (see

797   Methods). For L_vP, precipitation anomalies are multiplied by the latent heat of vaporization, L_v.

798   Radiative terms are computed with all-sky fluxes. The statistics of the linear regression (slope

799   [temperature-mediated response, W m^{-2} K^{-1}] and y-intercept [rapid adjustment, W m^{-2}]) are

800   displayed in the legend. Correlation coefficients of the scatterplots are ~0.99 for all terms except

801   SH, where it is -0.85.

802

803 **Extended Data Figure 2. Summary of model spread in temperature-mediated responses.**

804 (a) The temperature-mediated response of each atmospheric energy budget term (Eq. 1) is shown

805 for each model as blue circles and the model mean as a red cross. Responses of the radiative

806 terms ($dLWC/dT$ and $dSWA/dT$) computed with all-sky fluxes or with clear-sky fluxes are

807 denoted with all- or clr-, respectively. The numbers above the abscissa are the cross-model

808 correlations between $L_v dP/dT$ and each other temperature-mediated response. (b) Scatterplot of

809 the all-sky versus clear-sky temperature-mediated *SWA* response.

810

811 **Extended Data Figure 3. Total changes and rapid adjustments for *$L_v P$* and *SWA*.** (a) The

812 total change in *$L_v P$* per unit warming (mean over years 131-150 of the abrupt4xCO2 simulation

813 minus the corresponding mean of the piControl simulation, normalized by 2-m air temperature

814 change, $L_v \Delta P / \Delta T$) versus total change in clear-sky *SWA* per unit warming ($\Delta SWA / \Delta T$). (b) The

815 rapid adjustment of *$L_v P$* versus rapid adjustment of clear-sky *SWA*.

816

817 **Extended Data Figure 4. Contributions of water vapor change to model spread in**

818 **temperature-mediated *SWA* response.** (a) The Gregory method (Methods) is applied to

819 anomalies of globally-averaged specific humidity (*q*) at standard atmospheric levels, total

820 column precipitable water (*PW*), and upper tropospheric precipitable water [*PW(500-200)*,

821 computed by vertically integrating *q* between 500 and 200 mb] to quantify the temperature-

822 mediated response of atmospheric water vapor for each model. The natural log was applied

823 before computing annual anomalies. For each quantity, the symbols (circle, diamond, square)

824 represent the model mean and the whiskers represent the full model spread. The globally-

825 averaged annual-mean clear-sky shortwave atmospheric *q* kernel (Methods) is overlaid (blue

826   curve). (b) The cross-model correlation between the responses of water vapor in panel (a) and

827   the temperature-mediated clear-sky *SWA* response ($dSWA/dT$) computed with model-produced

828   fluxes (black) or radiative kernels (blue). Filled symbols are statistically significant at the 5%

829   level based on a two-tailed t-test[33], with degrees of freedom corresponding to the number of

830   participating modeling institutions (14) within the 25 model ensemble.

831

832   **Extended Data Figure 5. The *SWA* sensitivity curve for each model.** Normalized bin-mean

833   *SWA* versus *PW* and corresponding linear fit (as in Fig. 3a) for each model (black dots/line), with

834   models sorted from (top left) smallest $dSWA/dPW$ (%/[kg m^{-2}], printed on every panel) to

835   (bottom right) largest $dSWA/dPW$. Dashed lines depict the 10th-90th percentile spread of *SWA*

836   within each *PW* bin, demonstrating the tight constraint *PW* places on *SWA*. Numbers next to

837   model names are those from Extended Data Table 1. On every panel, the *SWA* versus *PW* curve

838   and linear fit based on CERES-EBAF fluxes and SSM/I water vapor are also shown (blue

839   triangles/line); the 10th-90th percentile spread is shown only on the second panel for visual

840   clarity.

841

842   **Extended Data Figure 6. Methodology for parameterizing absorption of solar radiation by**

843   **water vapor.** The relationship between $dSWA/dPW$ and methodology used to parameterize

844   solar absorption by water vapor in a cloud-free atmosphere, with colors for each model referring

845   to different parameterization procedures as documented in the references listed in the legend (see

846   also Extended Data Table 1). Boxes outlined in black indicate that water vapor continuum

847   absorption in the shortwave is accounted for in the parameterization. Model numbers are

848   defined. The width of the horizontal shading for each model represents the 95% confidence

849   interval of the regression slope to the *SWA* versus *PW* curve, as in Fig. 4. Statistical uncertainty

850   of $dSWA/dPW$ derived from CERES-EBAF fluxes and three *PW* datasets (obs) and from

851   ISCCP-FD is represented with vertical dashed lines, as described in Figs. 3 and 4, respectively.

852

853   **Extended Data Figure 7. Constraining the spread in late 21st century precipitation change.**

854   (a) The relationship between temperature-mediated clear-sky *SWA* response ($dSWA/dT$) and

855   *SWA* sensitivity to varying *PW* ($dSWA/dPW$) (as in Fig. 3b) showing an estimate of the "true"

856     $dSWA/dT$ (blue line/star), and how it is quantified. (b) The temperature-mediated L_vP response

857   ($L_v dP/dT$) versus $dSWA/dT$ (as in Fig. 2b) showing how the "true" $dSWA/dT$ in (a) is used

858   to quantify a bias in $L_v dP/dT$ originating from a bias in $dSWA/dT$; the bias for an example

859   model (#13: GISS-E2-R) is displayed. (c) The full (abscissa) versus constrained (with bias in

860   panel [b] removed, ordinate) total change (indicated with Δ) in L_vP normalized by change in 2-m

861   warming at the end of the 21st century under RCP8.5 (see Methods and Eq. 2). (d) As in (c) but

862   for total L_vP change not normalized by warming. Model numbers are defined in Extended Data

863   Table 1. Two models (#8: CNRM-CM5-2 and #23: MPI-ESP-P) are excluded from panels (c)

864   and (d) due to unavailable RCP8.5 output.

865

866

a

TOA ┈┈┈┈┈┈┈┈┈┈┈┈┈┈┈┈┈┈┈┈┈┈┈┈┈┈┈
LW_u SW_d SW_u

$LWC = (LW_u)_{TOA} + (LW_d-LW_u)_{SFC}$

$SWA = (SW_d-SW_u)_{TOA} - (SW_d-SW_u)_{SFC}$

SFC | L_vP LW_d LW_u SW_d SW_u SH
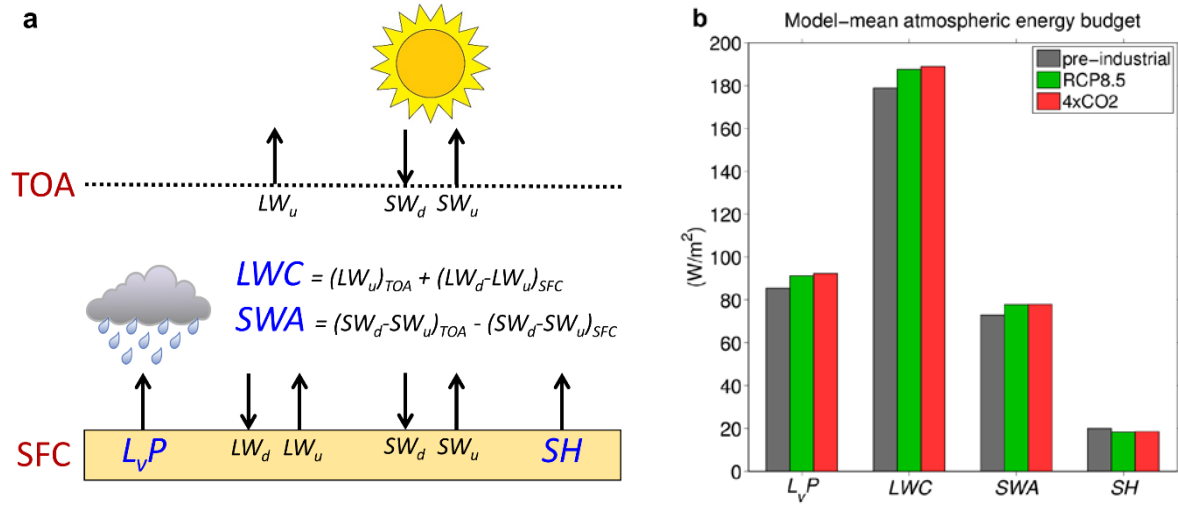
b   Model–mean atmospheric energy budget

867

Figure 1. The atmospheric energy budget. (a) Schematic of the fluxes considered in the budget. All fluxes (arrows) shown in the schematic are defined positive; some represent downward (denoted with subscript d) and others upward (denoted with subscript u) fluxes at the top-of-atmosphere (TOA) or surface (SFC). All flux arrows are drawn with the same length for simplicity. The four main energy budget terms considered in this study (Eq. 1) are identified with blue text. Two of them are radiative and are derived from individual longwave (LW) or shortwave (SW) flux components, following the equations in panel (a): net atmospheric longwave cooling (*LWC*, the sum of upward LW flux at TOA and net downward LW flux at the SFC) and shortwave absorption (*SWA*, net downward SW flux at TOA minus net downward SW flux at the SFC). The other two are the latent heat release from precipitation (L_vP, latent heat of vaporization multiplied by precipitation rate) and sensible heat flux from the surface to atmosphere (*SH*). (b) The global-mean values of the four terms simulated by the CMIP5 ensemble for the pre-industrial control simulation (average over 150 years), Representative Concentration Pathway scenario 8.5 (RCP8.5, average over 2091-2100), and abrupt quadrupled CO_2 scenario (average for years 141-150 after CO_2 quadrupling in all models except

883   CNRM-CM5-2 and IPSL-CM5A-MR, where it is for years 131-140). The model mean is shown

884   in all cases, and the radiative terms are computed using all-sky fluxes. All terms are positive.
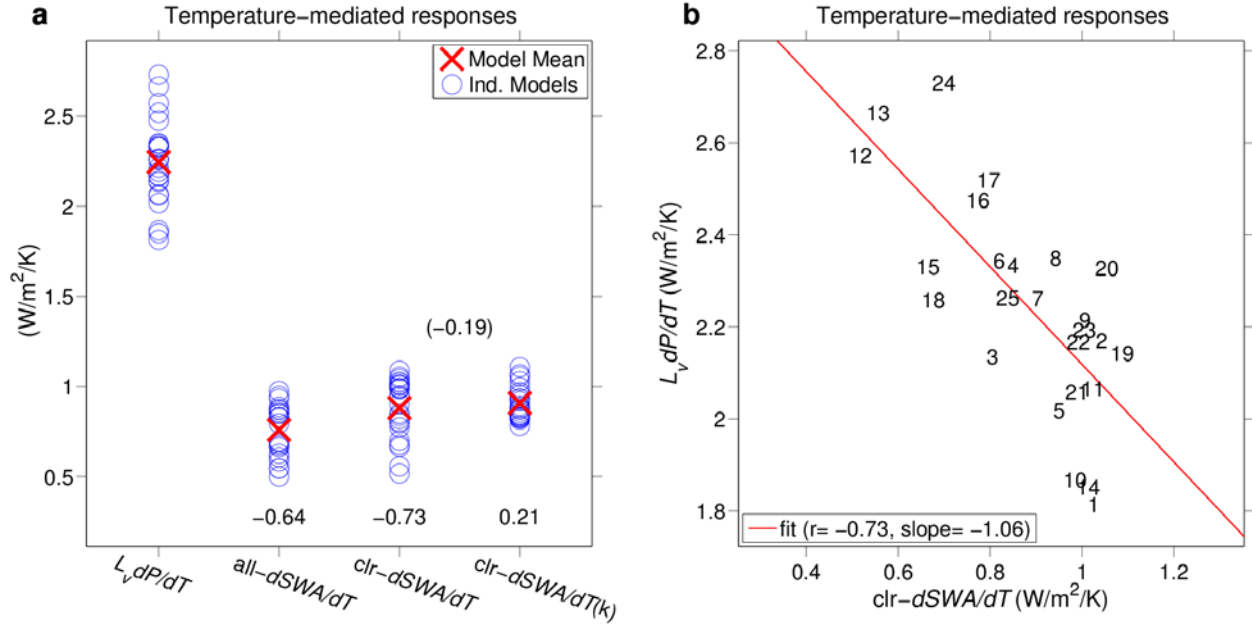
885

886

887

Figure 2. Relationship between temperature-mediated L_vP and SWA responses. (a) The temperature-mediated responses of L_vP ($L_v dP/dT$) and SWA ($dSWA/dT$) for all-sky (indicated with all-) and clear-sky (indicated with clr-) are shown. The values are computed using model-produced fluxes (as in Extended Data Fig. 1) except in the case of clr-$dSWA/dT$(k), in which they are computed with radiative kernels (Methods). Individual CMIP5 models are shown as blue circles. The numbers above the abscissa are the cross-model correlations between $L_v dP/dT$ and each $dSWA/dT$. The number in parentheses is the correlation between model-produced and kernel-derived clear-sky $dSWA/dT$. (b) Scatterplot of the model-produced $L_v dP/dT$ vs. clear-sky $dSWA/dT$ for the 25 models. Note that the abscissa and ordinate axes have the same scale. Model numbers are defined in Extended Data Table 1.
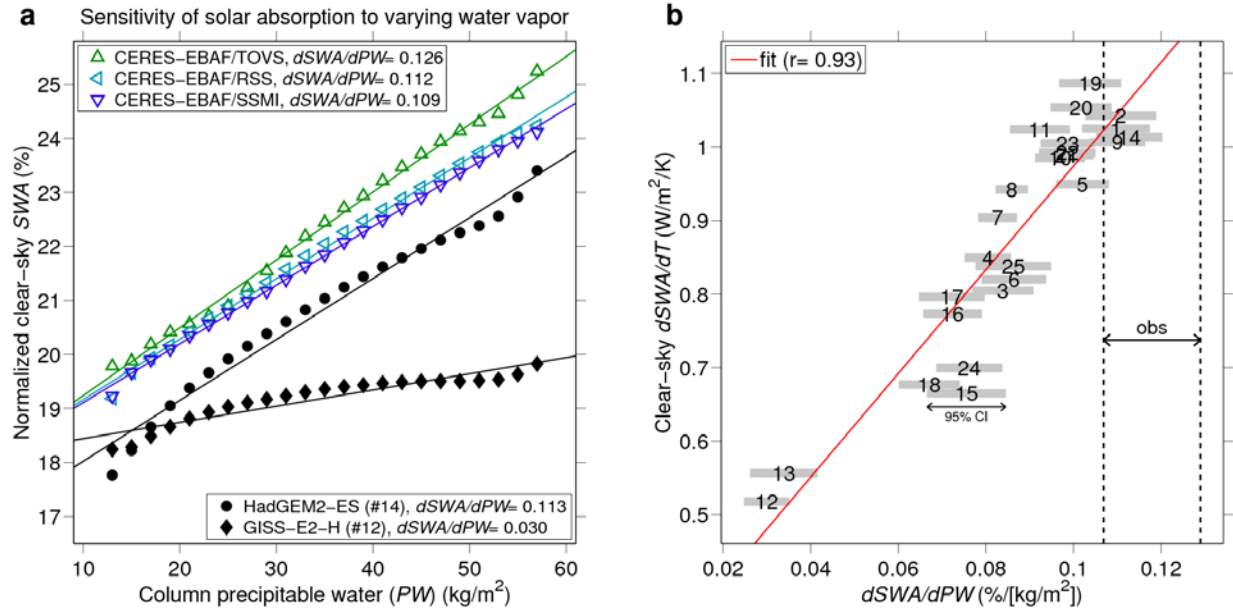
898

899

Figure 3. The sensitivity of solar absorption to varying atmospheric water vapor. (a) Clear-sky *SWA* normalized by incoming solar flux versus column precipitable water (*PW*) in the pre-industrial climate for selected models and for CERES-EBAF estimates with three *PW* datasets (see Methods). The slope of the curve represents the sensitivity of *SWA* to varying *PW* ($dSWA/dPW$) and its value is given in the legends for each model/dataset (%/[kg m^{-2}]). (b) Scatterplot of the (clear-sky) temperature-mediated *SWA* response to CO_2 forcing, $dSWA/dT$ (Fig. 2b), versus $dSWA/dPW$ (panel a) for the 25 models. In (b), the width of the horizontal shading for each model represents the 95% confidence interval (CI) of the regression slope to the *SWA* versus *PW* curve (Methods). Statistical uncertainty of the CERES-EBAF $dSWA/dPW$ estimate combining all *PW* datasets is shown with vertical dashed lines (obs). It is computed by (1) calculating the 95% CI of the slope of the CERES-EBAF curve with each individual *PW* dataset, then (2) calculating the absolute minimum to maximum of the three CIs (i.e., the minimum of the lower bounds of all CIs to the maximum of the upper bounds of all CIs).
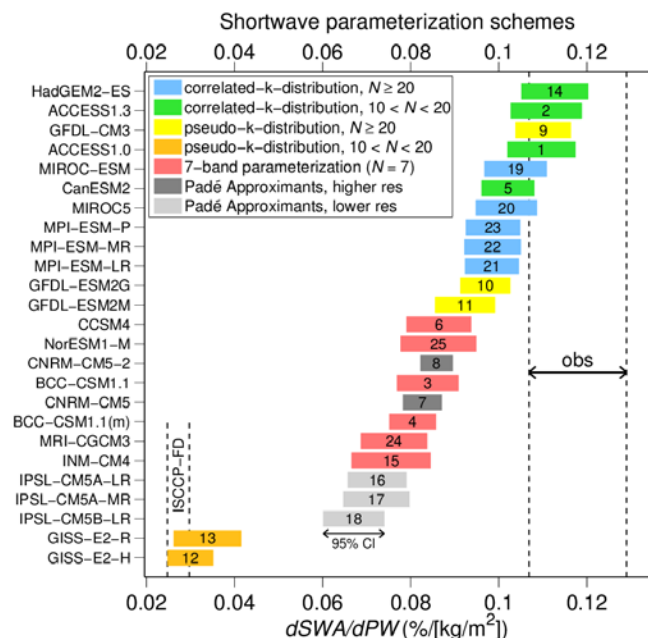
913

42

914

Figure 4. Shortwave parametrization schemes. The relationship between $dSWA/dPW$ (Fig. 3)

and characteristics of the parameterization scheme for solar absorption by water vapor in a

cloud-free atmosphere, with colors for each model referring to different types of

parameterizations as described in the legend (N refers to the number of exponential terms

representing water vapor absorption). References and further discussion are given in Extended

Data Table 1 and Methods, respectively. Model numbers are identified. The width of horizontal

shading for models and the vertical dashed lines for observations (obs) represent statistical

uncertainties of $dSWA/dPW$, as described in Fig. 3. The 95% CI for an estimate of

$dSWA/dPW$ based on ISCCP-FD (Methods) is also shown with vertical dashed lines.